Preparation of oxygen-sensitive proteins for high-resolution cryoEM structure determination using (an)aerobic blot-free vitrification

Brian D. Cook[1†], Sarah M. Narehood[1†], Kelly L. McGuire[1†], Yizhou Li[1], F. Akif Tezcan[1], Mark A. Herzik, Jr.[1⋆]

† These authors contributed equally

[1]Affiliations: Department of Chemistry and Biochemistry, University of California, San Diego, California, USA

⋆Correspondence: mherzik@ucsd.edu

Abstract: High-quality grid preparation for single-particle cryogenic electron microscopy (cryoEM) remains a bottleneck for routinely obtaining high-resolution structures. The issues that arise from traditional grid preparation workflows are particularly exacerbated for oxygen-sensitive proteins, including metalloproteins, whereby oxygen-induced damage and alteration of oxidation states can result in protein inactivation, denaturation, and/or aggregation. Indeed, 99% of the current structures in the EMBD were prepared aerobically and limited successes for anaerobic cryoEM grid preparation exist. Current practices for anaerobic grid preparation involve a vitrification device located in an anoxic chamber, which presents significant challenges including temperature and humidity control, optimization of freezing conditions, costs for purchase and operation, as well as accessibility. Here, we present a streamlined approach that allows for the (an)aerobic vitrification of oxygen-sensitive proteins using an automated aerobic blot-free grid vitrification device – the SPT Labtech chameleon. This robust workflow allows for high-resolution structure determination of dynamic, oxygen-sensitive proteins, of varying complexity and molecular weight.

Introduction

Metalloproteins are critically important for numerous biological processes, including electron transport in mitochondria, photosynthesis, and nitrogen fixation, and understanding their structures and functions remains critically important.[1–3] A large subset of these vital protein complexes harbor metal clusters that are susceptible to damage or altered function upon exposure to dioxygen (O_2).[4,5] Structural characterization of these O_2-sensitive metalloproteins has been hampered since they require specialized anaerobic setups and methodologies due to the risk of potentially obtaining results that inaccurately represent their functional states.[6,7] Indeed, the determination of the structures of such metalloproteins using X-ray crystallography requires crystallogenesis to occur under anaerobic conditions, typically requiring crystal trays to be in an anaerobic chamber for growth and harvesting.[8] Although there have been many successes using such approaches,[9–14] the conditions required for crystallization often precludes visualizing these complexes under catalytic turnover conditions due to the inherent dynamics frequently required for such processes and the timescales for crystal growth. As has been recently shown for several proteins, including the metalloenzyme nitrogenase, cryogenic electron microscopy (cryoEM) is well-suited to capturing O_2-sensitive metalloproteins under catalytic turnover conditions,[15–18] provided that the significant challenges for the preparation of cryoEM samples in anaerobic conditions can be overcome.

In the past decade, significant technological advances in microscope hardware and data processing algorithms have established cryoEM as a leading technique for macromolecular structure determination.[19] While these technological advances continue to pay dividends with near-exponential growth in the number of structures determined by cryoEM each year, sample preparation remains a key bottleneck.[20,21] The unpredictable nature of cryoEM sample vitrification frequently results in partial or complete destabilization of samples, preferential orientation, or inconsistent freezing behavior.[20,22–24] Notably, these issues are exacerbated in the case of O_2-sensitive samples that require anaerobic handling conditions as O_2exposure can result in oxidation and/or loss of metal/cofactors, loss of activity, and even protein denaturation.[4,5,25,26] To date, cryoEM structure determination of anaerobic proteins has required custom sample preparation setups and/or specialized equipment.[15,16] Indeed, to address the multitude of challenges associated with preparing cryoEM grids anaerobically, several recent studies have approached these challenges by conducting this process in an anoxic environment, such as an anaerobic chamber, or by protecting the sample from O_2 once relocated to an aerobic environment.[15,16] While dedicating a cryoEM grid preparation device within an anaerobic chamber is an effective strategy to limit or eliminate O_2 during cryoEM grid preparation, this approach is costly and lack of accessibility prevents widespread adoption across the community. Establishing a standardized workflow for freezing O_2-sensitive proteins

using grid preparation devices readily available at cryoEM facilities would facilitate broadscale adoption in a critical area of structural biology.

Here, we present a novel workflow that utilizes the SPT Labtech chameleon – a next-generation nanospray cryoEM grid preparation device – in an aerobic environment to freeze O_2-sensitive proteins under functionally anaerobic conditions, which we term (an)aerobic. Our workflow maintains (an)aerobic samples by protecting against or eliminating O_2 contamination prior to loading into the chameleon, during sample aspiration, and throughout sample deposition on self-wicking EM grids, respectively. Demonstrating the utility of this workflow, we determined high-resolution cryoEM structures of deoxygenated human hemoglobin (Hb) and the molybdenum-iron protein (MoFeP) – the O_2-sensitive catalytic component of *Azotobacter vinelandii* nitrogenase – in a reduced state. Finally, we detail the effects of O_2 contamination at different stages of the workflow and show how to prevent their effects. Together, we demonstrate reproducible high-resolution structure determination of O_2-sensitive proteins of varying complexity and size – as small as 64 kDa – with a workflow requiring only minimal modifications to a robust, widely available EM grid freezing method.

Results

Development of a specialized workflow for freezing (an)aerobic samples using the SPT Labtech chameleon.

While standard cryoEM grid preparation by blot-and-plunge freezing has remained essentially unchanged for decades, a new generation of sample preparation devices uses nanoliter sample dispensing heads and self-wicking cryoEM grids to automate sample preparation. These devices, including Spotiton and the SPT Labtech chameleon, enable precise control over ice thickness and also potentially address air-water interface issues and preferred-orientation problems.[27–32] This vitrification method has the potential to enhance and modernize current freezing practices for studying challenging proteins, and has been demonstrated to enable freezing of unstable or sensitive proteins.[32–34] We sought to adapt the aerobic chameleon grid vitrification protocol for anaerobic samples by systematically addressing key stages of the workflow where O_2 could contaminate the sample. These stages include: (1) pre-loading, during which the sample is exposed to O_2 before loading into the chameleon's piezo-electric dispenser, (2) pre-deposition, during which O_2 may enter the piezo-dispenser before sample deposition onto the EM grid, and (3) post-deposition, where O_2 exposure may occur during the auto-wicking process on the EM grid prior to vitrification.

We chose an O_2-binding protein, human hemoglobin (Hb), as a model system for development of an (an)aerobic workflow for sample preparation in the chameleon **(Figure 1A)**. Briefly, Hb is a heterotetramer ($\alpha_2\beta_2$) with each subunit harboring a heme cofactor that is capable of binding O_2 in solution when the heme iron is in a ferrous (Fe^{2+}) state.[35,36] Importantly, the oxidation and ligand-bound states of Hb can be readily monitored using UV-vis spectroscopy **(Figure 1B)** and further verified using cryoEM.[37–39]

We first elected to limit the amount of O_2 that enters the sample prior to loading in the chameleon dispenser. Briefly, to prepare EM grids using the chameleon, the isolated protein sample must first be transferred into a dedicated single-use chameleon sample cup and then placed into the instrument for aspiration into the dispenser. For aerobic samples, this process can readily be performed at the instrument immediately prior to vitrification.[33] To achieve this same process for anaerobic samples, there needs to be a mechanism to prevent or limit O_2 perfusion into the sample before aspiration. To achieve this, we elected to add a protective O_2 barrier containing a 50:50 mixture of paraffin oil and silicon oil (a.k.a. Al's oil) directly on top of the sample **(Figure 1A, 1C, and Fig. S1)**.[40–42] Due to the physical properties of the oil layer, O_2 perfusion into the anaerobic sample should be slowed and therefore help to maintain anaerobic conditions until sample aspiration.[43] To verify this, we prepared deoxygenated Hb by resuspending lyophilized human methemoglobin (metHb) in 1x phosphate-buffered saline (PBS) and then reducing the hemes in metHb from the ferric Fe^{3+} state to the ferrous Fe^{2+} state (deoxygenated Hb; herein referenced as deoxyHb) using the chemical reductant, sodium dithionite (NaDT), in an anaerobic chamber. As monitored by UV-vis spectroscopy, metHb has a Soret maximum at 405 nm indicating that the heme Fe is in an oxidized state (Fe^{3+}) and incapable of binding O_2. When the Fe centers are reduced (Fe^{2+}) using NaDT, a noticeable shift in the Soret maximum to 430 nm occurs while a broad peak is detected at 550 nm **(Figure 1B)**.[44] We then placed 1 ml of deoxyHb into a cuvette and added anaerobic Al's oil on top to the same approximate height of the chameleon sample cup (∼5 mm). We then monitored O_2 binding to deoxyHb by measuring the change in absorbance at 415 nm – the Soret maximum of O_2 - bound Hb (oxyHb) – following exposure to O_2 **(Figure 1B,1C, and Fig. S2)**.[44] Notably, this sample was able to remain deoxygenated under air for up to 20 minutes. However, when compared to the same deoxyHb sample without the protective oil layer, O_2 binding occurred much more rapidly, indicating that the oil layer is a sufficient first line of protection **(Figure 1C and Fig. S2)**. Although these conditions do not perfectly mimic those the sample will experience in the chameleon sample cup, the extent of protection that the anaerobic oil layer provides should be similar.

During sample aspiration, the chameleon dispenser needs to penetrate through the protective oil layer to access the sample at the bottom of the chameleon sample cup **(Figure 1A)**. Immediate inspection of the dispenser tip in the chameleon software after this step indicates residual oil remains on the outside of the tip, likely affecting the dispensing efficiency **(Fig. S1)**. To remedy this problem, we incorporated additional dispenser wash steps to remove any residual oil and restore normal dispenser behavior **(Fig. S1 and Methods)**. Although these steps can be performed quickly, we wanted to ensure that this would not lead to potential

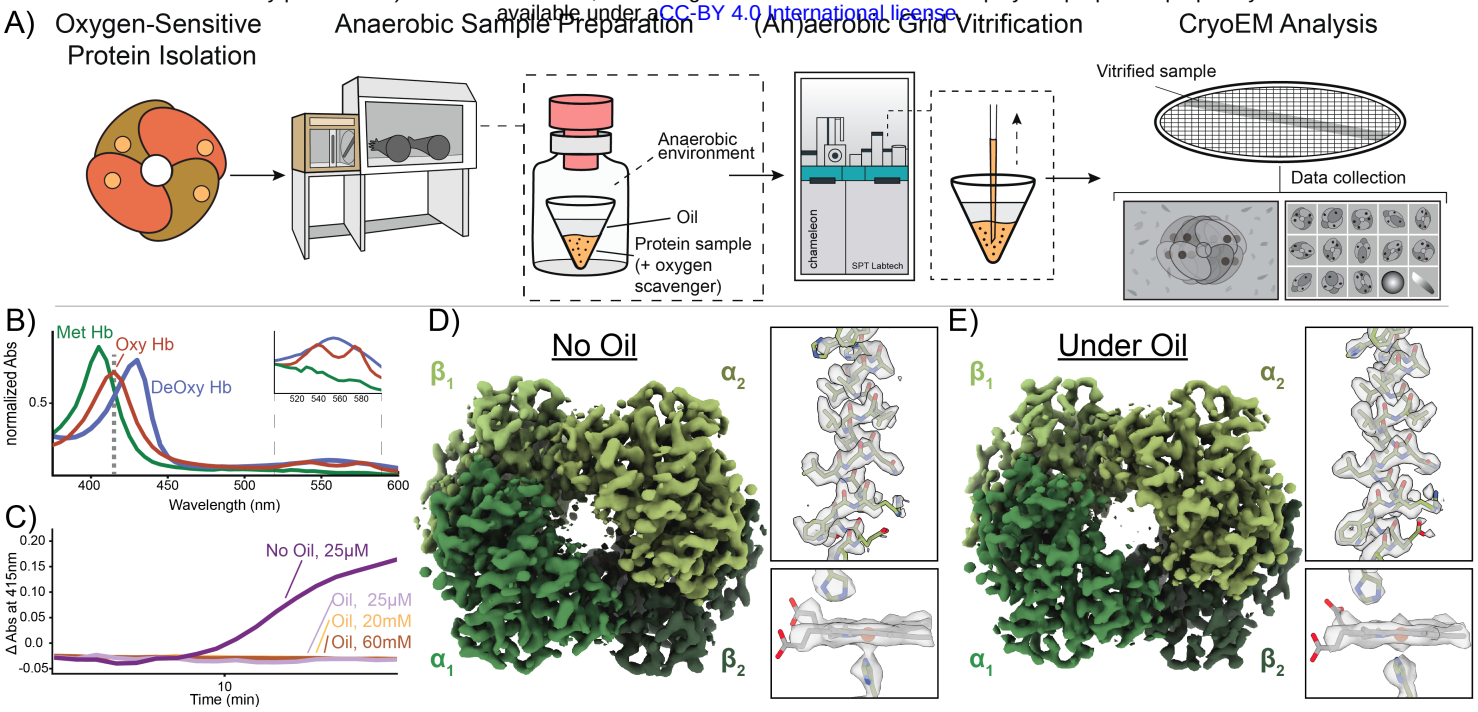

Figure 1: Development of the (an)aerobic SPT Labtech chameleon grid vitrification protocol. A) Schematic of the (an)aerobic cryoEM grid vitrification protocol using the SPT Labtech chameleon. In an anaerobic environment, the O_2-sensitive sample is placed into the chameleon sample cup and then covered with a layer of anaerobic Al's oil to protect the sample from O_2. The sample cup is then transferred into a glass vial and sealed for transport to the chameleon for preparation of high-quality grids. **B)** UV-VIS analysis of the different human Hb oxidation and liganded states discussed in this study. Methemoglobin (metHb, green line), deoxyHb (blue line), and oxyHb (red line) have distinct Soret peak maximums at 405 nm, 430nm, and 415 nm, respectively. Dashed line represents abs (415nm) monitored in **C**. **C)** O_2 titration curves of deoxyHb with varying NaDT concentrations and with or without the presence of Al's oil. **D-E)** Comparison of metHb densities determined with or without the protective Al's oil layer detailing no obvious differences in the metHb densities between the sample with oil present or not. For each structure, zoomed-in views of alpha helix 100-118 and the heme cofactors of subunit β_1 detail high-quality of both reconstructions.

issues in dispenser operation, sample deposition on the EM grid, and/or a decrease in sample integrity. To eliminate these possibilities, we next assessed the effect of the protective oil layer on grid preparation and downstream cryoEM imaging and data processing using our metHb sample. Briefly, we created two metHb samples – one without and one with the protective oil layer – by placing 15 μL of metHb ($\sim$125 μM) each into two sample cups. One sample was used without modification (non-oiled) and $\sim$70 μL of aerobic Al's oil was carefully layered over the second sample up to the brim of the sample cup (oiled). Two cryoEM grids of each sample were prepared using the chameleon following recommended guidelines.[33] Both metHb samples were imaged using the same microscope parameters with approximately the same number of micrographs for each dataset collected **(see Methods)**. We did not observe any noticeable differences neither in the quality of the sample stripes on the grids nor in their behavior during data collection. Both datasets were processed independently but with similar steps and parameters to allow for a direct comparison of the resulting densities **(Fig. S3)**. Comparison of our 2.78-Å resolution non-oiled and 2.71-Å resolution oiled metHb EM densities did not indicate any notable differences in their overall quality **(Figure 1D-E)**. Indeed, the view distribution and the total number of particles were similar between the samples, each resolved to similar resolution, and demonstrated similar map-to-model validation metrics **(Figure 1D-E, Fig. S3 and Table 1)**. Thus, the addition of Al's oil to protect the sample during chameleon grid preparation does not significantly hinder operation of the chameleon nor our ability to obtain high-resolution structures.

CryoEM structures of oxy, mixed, and deoxy hemoglobin to assess the anaerobic chameleon workflow.

A major source of potential O_2 contamination is the transportation from the anaerobic chamber to the chameleon. To address this issue, we placed the oil-layered sample inside a gas-tight glass vial (e.g., Reacti-vial) and sealed it with a rubber septum inside the anaerobic chamber to preserve the anoxic environment. Notably, the samples must remain stored in this condition until the chameleon is ready for sample aspiration. Once the chameleon is ready for sample loading, the septum is removed and the chameleon sample cup containing the protective oil-layered sample is carefully transferred from the glass vial to the chameleon sample cup holder and immediately aspirated into the chameleon dispenser **(Figure 1A and Fig. S1)**. EM grid preparation can then be performed normally **(Figure 1A)**.[33] We surmised that the oil layer alone would not be sufficient to eliminate O_2 introduction into the sample, so we decided to incorporate additional measures to eliminate O_2 perfusion into the sample during grid freezing and determine the structure of deoxyHb as our O_2 sensor. Specifically, we sought to address potential O_2 contamination in our samples during the vitrification process by simultaneously optimizing the critical 'wicking period' following sample deposition onto the grid

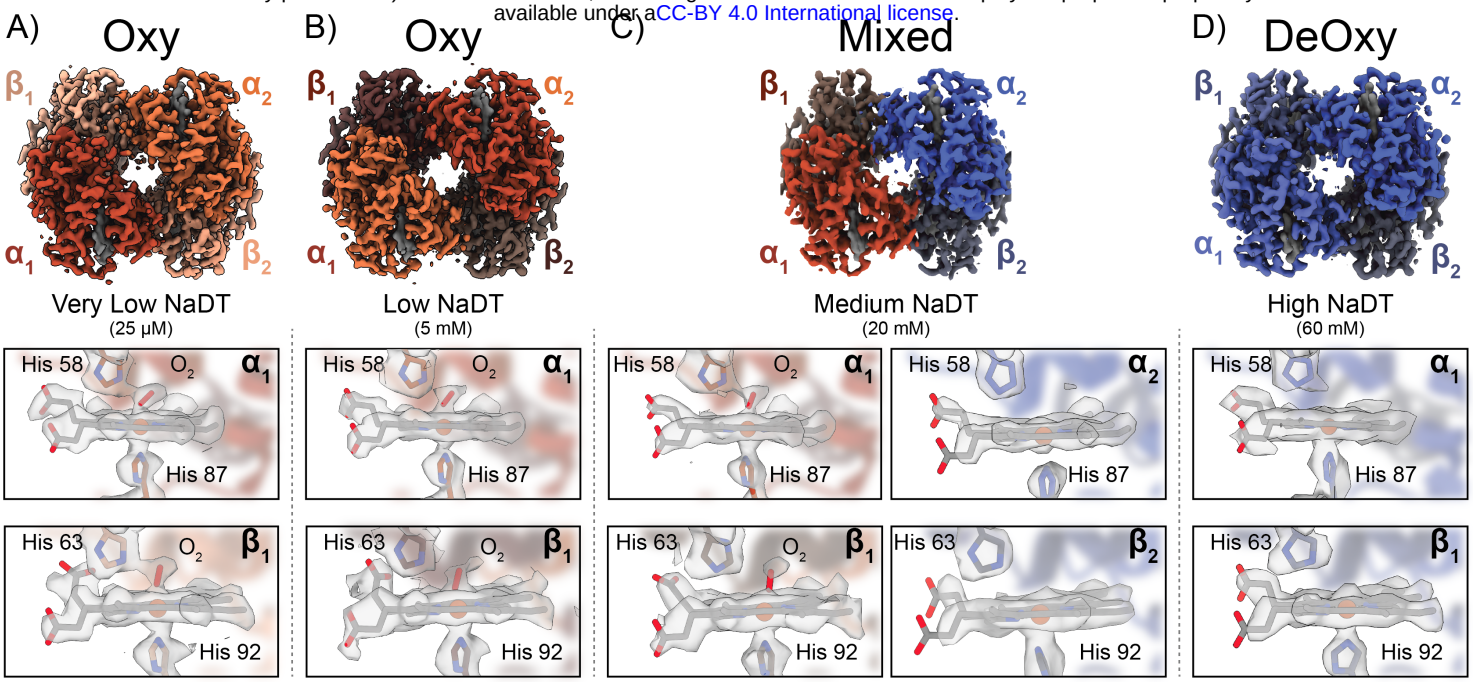

Figure 2: CryoEM structures of various Hb species using the (an)aerobic chameleon protocol. A) 2.4-Å resolution cryoEM structure of oxyHb (C2 symmetry applied) determined under 25 /*mu*M NaDT. Zoomed in views (shown below) of the α_1 and β_1 heme cofactors indicate clear density of bound O_2 above the Fe of each heme. **B)** 2.4-Å resolution cryoEM structure of oxyHb (C2 symmetry applied) determined under 5 mM NaDT. Zoomed in views (shown below) of the α_1 and β_1 heme cofactors indicate clear density of bound O_2 above the Fe of each heme **C)** 2.7-Å resolution cryoEM structure of a partially oxygenated Hb species (C1 symmetry applied) obtained under 20 mM NaDT. Clear O_2 density was found above the α_1 and β_1 heme groups while the α_2 and β_2 heme groups lacked any such density. **D)** 2.7-Å resolution cryoEM structure of deoxyHb under 60 mM NaDT.

necessary for sufficiently thin ice in our cryoEM samples and the necessary concentration of NaDT – a versatile reducing agent that is also capable of depleting solutions of dissolved O_2 – in the sample buffer required to maintain anaerobic conditions.[45] Importantly, the wicking time is a key variable during grid preparation using the chameleon as this phase significantly influences the uniformity and thinness of the resultant ice layer and can be easily tuned by the user: too short and the ice will be too thick for ideal imaging, and too long and this will lead to complete oxygenation of the sample and potentially yield too thin an ice layer. By balancing the NaDT concentrations and the wicking time, we sought to determine the cryoEM structure of deoxyHb.

To begin to explore the relationship between [NaDT] and wicking time, we first prepared deoxyHb in PBS buffer supplemented with 25 μM NaDT (here termed very low NaDT). Although this concentration of NaDT is an order of magnitude below the predicted concentration of O_2 (250 μM) in solutions prepared under ambient atmosphere, we included it to ensure that all hemes remained in the ferrous state after initial preparation of deoxyHb and buffer exchange. We then transferred the deoxyHb sample from the anaerobic environment to the chameleon using the protective oil layer conditions described above **(Figure 1A)** and prepared EM grids using similar conditions and wicking times as our metHb samples. We then determined the structure of this very low NaDT Hb at a resolution of 2.37-Å **(Figure 2A, Fig. S4, and Table 1)**. This structure revealed that Hb was in the relaxed (R) conformation (as indicated by the rotation of $\alpha_1\beta_1$ in relation to the $\alpha_2\beta_2$), which is the form of Hb with a high affinity of O_2.[35] Evaluation of the heme pocket for each subunit indicated a density above each heme that was not present in our metHb structures, consistent with molecular O_2 binding to the Fe centers **(Figure 1D-E and Figure 2A)**. The O_2-heme coordination metrics and geometries closely correspond to those observed in the X-ray structures of oxyHb **(Fig. S5)**.[46] Additionally, we used phenix.resolve_cryo_em – a cryoEM density modification tool adapted from X-ray crystallography – to better visualize the O_2 density above the hemes **(Figure 2A)**.[47] This dataset demonstrated that during sample deposition and self-wicking, O_2 exchanges rapidly enough for Hb to bind it. Thus, determining a NaDT concentration sufficient to maintain anaerobic conditions is critical.

To find a concentration of NaDT that would protect our sample from O_2 contamination while also allowing for proper biological function, we determined the structure of deoxy-Hb at different NaDT concentrations. Given that concentration of dissolved molecular O_2 is approximately 250 μM, we used a NaDT concentration of 5 mM to potentially capture any O_2 exchanging during sample deposition and wicking. Using similar conditions as the no-NaDT oxyHb, we generated a Hb sample under anerobic conditions supplemented with 5 mM NaDT (termed "low NaDT") and used approximately the same wicking time as our no-NaDT oxyHb. We transported this sample under oil and in the gas-tight vial to the chameleon. Following grid preparation, we collected a dataset of this low-NaDT sample and determined a 2.47-Å resolution structure of Hb **(Figure 2B, Fig. S6, and Table 1)**. Interestingly, this Hb structure once again had similar densities of heme-bound O_2's at every heme within the tetramer sim-

ilar to the very low NaDT oxyHb sample. Additionally, the low-NaDT Hb tetramer was in the R state and the refined models matched previous O_2-heme coordination geometries **(Fig. S5)**. Although the concentration of NaDT used in this sample was an order of magnitude higher than the theoretical dissolved O_2 concentration, we reasoned that decreasing the sample wicking time while simultaneously increasing the NaDT concentration should prevent O_2 contamination.

We next sought to decrease the wicking time used in our metHb/oxyHb structures (from ∼900 ms to ∼300 ms) to limit the total time the sample was exposed to air after deposition onto the grid, while also increasing the [NaDT] to 20 mM (termed "medium NaDT") to deplete any O_2 entering the sample. DeoxyHb was prepared similarly as described above and exchanged into PBS supplemented with 20 mM NaDT prior to transporting under oil and transfer to the chameleon. We prepared cryoEM grids using our modified (an)aerobic chameleon protocol **(Figure 1A and Methods)** and collected a similarly-sized dataset as metHb/oxyHb to determine a 2.56-Å resolution structure of Hb **(Figure 2C, Fig. S7, and Table 1)**. Remarkably, when compared to our oxyHb structure, the densities of the heme-bound O_2's were weaker and displayed heterogeneity across the different hemes. Specifically, we observed that the α_1 and β_1 hemes showed bound O_2, while the α_2 and β_2 hemes lacked any such density **(Figure 2C)**. The densities in the α_1 and β_1 subunits are similar in nature to those observed in our oxyHb structure and indicate that they are most likely molecular O_2 with the α_2 and β_2 hemes in the unliganded state **(Fig. S5)**.

The above data suggest that 20 mM NaDT provided some protective effect but did not completely eliminate O_2 perfusion into the sample during sample deposition and vitrification, despite the shortened wicking time used for this sample. As wicking time could not be further reduced without resulting in unacceptably thick ice for such a low molecular weight sample, we increased the final concentration of NaDT to 60 mM (termed "high NaDT") to ensure complete elimination of contaminating O_2. We prepared deoxyHb in the same manner described above in PBS supplemented with 60 mM NaDT in the final buffer and prepared cryoEM grids using identical conditions as the mixed-O_2 species **(Table 1)**. We collected a dataset of similar size and determined the structure Hb to a resolution of 2.61-Å **(Figure 2D, Fig. S8, and Table 1)**. Although the overall tetramer structure was once again R state, our analysis of the heme groups in each subunit revealed an absence of any density stretching above the Fe, indicative of O_2 binding, within the hemes. Additionally, when we fit a previously determined deoxyHb atomic model into the density, a well-defined water found in the X-ray model fits into a density above the heme **(Fig S9)**. Together, these structures indicate that, in combination, the protective oil layer, minimized sample wicking times, and appropriate [NaDT] are sufficient to maintain deoxyHb until structure determination and therefore create sufficiently functionally anaerobic conditions for O_2-sensitive samples.

CryoEM structures of Azotobacter vinelandii MoFe protein (MoFeP) under (an)aerobic conditions.

Having demonstrated the effectiveness of our protocol in (an)aerobically preparing cryoEM grids for the determination of deoxyHb structure using the chameleon, we next targeted the nitrogenase MoFeP– an O_2-sensitive metalloenzyme that plays a pivotal role in converting atmospheric dinitrogen (N_2) to ammonia (NH_3).[1,48] Despite decades of research, there continue to be numerous outstanding questions pertaining to the structural intermediates of biological N_2 fixation that remain unanswered due to limitations in structural techniques for investigating O_2-sensitive enzymes.

Nitrogenase comprises two subunits: the reductase subunit, known as iron protein (FeP), and the catalytic subunit, known as MoFeP. MoFeP is a heterotetramer ($\alpha_2\beta_2$) composed of two symmetry-related $\alpha\beta$ dimers, each containing an [8Fe:7S] electron-relay cluster (P-cluster) and a [7Fe:1Mo:9S:1C] catalytic cofactor (FeMoco). Due to the sensitivity of these metal clusters, most structural studies of nitrogenase have been performed through anaerobic X-ray crystallography.[49–52] While informative, X-ray crystallography is not ideally suited to capture transient catalytic states associated with large conformational changes, which is the case in nitrogenase. Recent studies of nitrogenase have used cryoEM to uncover important dynamic steps within the nitrogenase cycle.[15,16] However, these studies relied on freezing techniques that are either difficult to replicate or require costly/laborious implementation of grid preparation devices in an anaerobic environment. Thus, we decided to use MoFeP to determine if our anaerobic freezing protocol can be used on a highly O_2-sensitive sample.

To demonstrate the O_2 sensitivity of MoFeP during traditional aerobic grid vitrification, we first froze cryoEM grids of NaDT-reduced MoFeP using similar conditions as deoxyHb but without the protective oil layer or NaDT in the cryoEM sample buffer. Using our chameleon protocol, we prepared grids of MoFeP and obtained a 2.39-Å resolution structure **(Figure 3A, Fig. S10, and Table 2)**. As expected from previous studies of nitrogenase under conditions of O_2 exposure, we did not see any obvious changes or damage to FeMoco **(Figure 3B)**, but an inspection of the EM density around the P-cluster suggested that it was in the 2-electron oxidized (P^{2+}) state, indicating O_2 perfusion through the sample **(Figure 3C)**. The P-cluster resembles two fused 4Fe:4S clusters and is responsible for electron transfer from the FeP to FeMoco during the catalytic cycle. However, the P-cluster is also highly sensitive to O_2 exposure and is rapidly oxidized under aerobic conditions that results in significant alterations to the metal cluster geometry and coordination. When the fully reduced (P^N) resting state of the P-cluster undergoes a one-electron oxidization to the (P^{1+}) state, the Fe6 atom that is initially coordinated to S1 in P^N becomes coordinated to a neighboring serine within the beta subunit (β^1S188) **(Figure 3C; red arrow)**. A further one-electron oxidation of the cluster to the (P^{2+}) state leads to the additional coordination

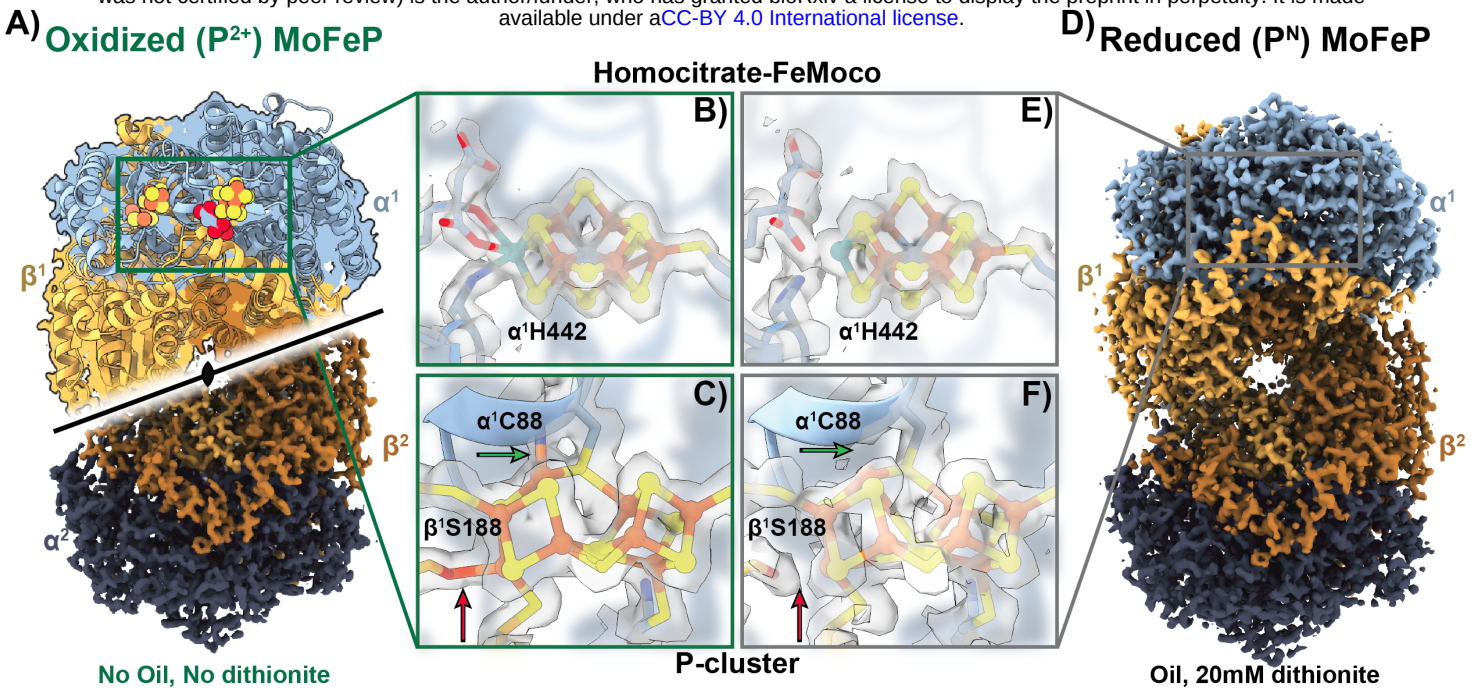

Figure 3: CryoEM structures of oxidized and reduced MoFeP. A) 2.4 Å cryoEM structure of oxidized (P^{2+}) *Av*MoFeP obtained using the chameleon aerobically (without protective oil or NaDT). The C2 symmetry axis is indicated. **B)** The EM density for the homocitrate-FeMoco ligand of the oxidized MoFeP does not exhibit significant change or damage. **C)** The oxidized P^{2+} P-cluster from the sample prepared aerobically (A) indicates clear density for linkages between the α^1C88 amide backbone nitrogen with Fe5 (green arrow) and the β^1S88 side-chain with Fe6 (red arrow) of the P-cluster. **D)** 2.1 Å cryoEM structure of reduced (P^N) AvMoFeP obtained using the (an)aerobic chameleon protocol with protective oil and 20 mM NaDT. **E)** Similar to B), the homocitrate and FeMoco do not show significant changes is the reduced MoFeP structure. **F)** The linkages indicative of oxygen damage are lacking in the anaerobically-prepared MoFeP indicating a reduced (P^N) P-cluster(red and green arrows). **B-C,E-F)** Surrounding residues were rendered transparent for clarity.

of the Fe5 atom to the amide backbone of one of the coordinating cysteines in the alpha subunit (α^1C88), which is accompanied by the dissociation of the bond between Fe5 and the bridging S1 sulfur atom **(Figure 3C; green arrow)**. Both of these linkages are present in our aerobically-prepared MoFeP structure, confirming oxidation of the P-clusters to the P^{2+} state following O_2 exposure during grid preparation **(Figure 3A and B)**.

We then prepared cryoEM grids of NaDT-reduced MoFeP using conditions similar to those used to obtain our deoxyHb structure, using a final [NaDT] of 20 mM **(Figure 3D, Fig. S11, and Table 2)**. Analysis of our 2.08-Å resolution anaerobic MoFeP cryoEM structure indicates an intact FeMoco **(Figure 3E)**. Additionally, we found a fully reduced P-cluster (P^N) was preserved with no evidence of density that would indicate the dissociation of the bonds to the bridging S1 or coordination with neighboring residues as observed in the P^{1+} and P^{2+} states **(Figure 3F, red and green arrows)**. The presence of this intact P-cluster paired with the high resolution of this structure indicates that this method is well-suited for reproducibly preparing functionally anaerobic cryoEM grids and obtaining high-resolution structures of O_2-sensitive proteins.

Discussion

The primary challenge in anaerobic protein preparation and cryoEM grid preparation lies in conducting both processes within an anaerobic environment (e.g., a glovebox/bag) or protecting a O_2-sensitive sample outside such an environment. Since most anaerobic purifications require careful handling within an anoxic environment, nearly all anaerobic cryoEM studies to date rely on relocating costly grid preparation devices into an anaerobic glovebox/bag. This approach creates several challenges. First, the temperature and humidity within an anaerobic chamber can be difficult to regulate. Also, the transport of materials into a glovebox/bag can be challenging and time consuming due to the requirement that each item that enters a glovebox/bag needs to undergo degassing cycles before it can enter the anaerobic environment. Here, we circumvent these problems by developing an (an)aerobic sample freezing protocol outside an anaerobic chamber using the SPT Labtech chameleon. We demonstrate the utility of this protocol by determining the high-resolution cryoEM structures of human deoxyHb and reduced *A. vinelandii* MoFeP, with both structures showing a lack of O_2 exposure during structure determination. During Hb preparation, we found that we could control the O_2 exposure in the samples by varying the concentration of NaDT in the cryoEM buffer. We observed that at NaDT concentrations below 5 mM, all four hemes within Hb were bound to O_2, while increasing [NaDT] to 20 mM or 60 mM led to either a partially-bound oxyHb structure or a fully deoxygenated Hb structure, respectively. Importantly, this is the first observation of a partially O_2-bound Hb structure with α_1 and β_1 hemes occupied. Similarly, for MoFeP, absence of the protective oil layer and NaDT in the cryoEM buffer yielded oxidized P-clusters, but addition of the protective oil layer and NaDT in the cryoEM buffer yielded reduced P-clusters.

During the optimization of our anaerobic chameleon protocol, we found a few key steps within the chameleon operation that limits issues encountered during freezing. First, while the chameleon requires at least 5 μL of sample for operation, we recommend that the minimum volume of sample placed within the sample cup be 15 μl with 7 μL of that 15 μl being drawn up into the dispenser since the chameleon aspirates sample from the bottom of the sample cup. The additional volume of sample ensures that any O_2 contamination remains at the top of the sample vial near the protective oil layer and never enters the dispenser tip. Another issue that we overcame was the protective oil layer remaining on the dispenser after sample aspiration. Any oil remaining on the outside of the dispenser can affect sample deposition and therefore needs to be removed. During regular chameleon operation, the user is prompted to test the dispenser once sample is aspirated. During this step, the user can re-prime the dispenser, increase sample application amplitude, and/or choose to clean and purge the system to remove debris. To ensure proper sample ejection after aspirating sample through the protective oil layer, we found that we needed to perform multiple cleaning steps and adjust the amplitude to achieve the desired dispensing result. In addition, we observed that the faster wicking time of 300 ms with adequate glow discharge was a good balance for obtaining sufficiently thin ice for high-resolution imaging. Furthermore, to limit the time the sample was exposed to O_2, we prioritized freezing grids within 90-120 s of aspiration and typically froze 1-2 grids per sample. Other than these changes, this protocol follows the same steps as an aerobic chameleon protocol and only requires 30-60 s additional operation time per grid prepared.

The SPT Labtech chameleon is an emerging technology that is being adopted around the globe into numerous cryoEM facilities, including the NIH-sponsored cryoEM national centers within the United States. We demonstrated how to adapt the chameleon workflow to keep samples (an)aerobic while generating high-quality grids amenable for high-resolution structure determination. Two primary modifications to the workflow – the protective oil layer and addition of oxygen scavenger – render this accessible instrument amenable to the freezing of anaerobic samples. By having the ability to simply layer one's sample with oil – which does not affect the quality of the prepared cryoEM grids – and supplement with a versatile chemical reductant, sodium dithionite, will allow any user studying oxygen-sensitive proteins to create high-quality cryoEM grids using this (an)aerobic blot-free vitrification protocol.

Methods

Preparation of human metHb for cryoEM analysis

Lyophilized human methemoglobin (Sigma Aldrich) (metHb) was resuspended in phosphate buffered saline (PBS; ThermoFisher) at pH 7.5 to a concentration of ∼10 mg/mL. The concentration and oxidation state were measured and confirmed, respectively, using an Agilent 8453 UV-Vis spectrophotometer.

Preparation of human deoxyHb for cryoEM analysis

MetHb was transferred into a Coy Laboratories anaerobic chamber (95% Ar, 5% H2) and briefly degassed. A stock solution of 1M sodium dithionite (NaDT) was prepared in 1M Tris-base. NaDT was added to metHb to a final concentration of 100 mM and allowed to incubate for 5-10 min in the glove bag. DeoxyHb was then desalted into anaerobic PBS buffer in the glovebag using a PD-10 desalting column. The concentration and oxidation state were measured and confirmed, respectively, using UV-Vis. DeoxyHb was then diluted with anaerobic PBS to a final concentration of 125 μM Hb supplemented with either 25 μM, 20 mM, or 60 mM NaDT.

Expression and purification of molybdenum iron protein (MoFeP) from Azotobacter vinelandii

Preparation of wild-type molybdenum iron protein (MoFeP) from *Azotobacter vinelandii* (*Av*MoFeP) (*Av* strain DJ200) was performed as previously detailed, and flash frozen under liquid nitrogen until use.[53]

CryoEM sample preparation

Hb Samples:

15 μL of human metHb (125 μM) was pipetted into a chameleon sample cup (SPT Labtech) and used for cryoEM grid preparation. 15 μL of human metHb (125 μM) was pipetted into a chameleon sample cup and ∼70 μL of Al's oil (Hampton Research) was carefully layered on top of the sample up to the brim of the sample cup and used for cryoEM grid preparation. In a Coy Laboratories anaerobic chamber (95% Ar, 5% H2), 15 µL each of deoxHb with 25 μM [NaDT], deoxyHb with 5 mM [NaDT], deoxyHb with 20 mM [NaDT], and deoxyHb with 60 mM [NaDT] were separately pipetted into their own chameleon sample cup located within a 3 mL glass, conical-bottom Reacti-Vial (Thermo Fisher Scientific). The chameleon sample cups had equilibrated in the anaerobic chamber overnight. ∼70 µL of anaerobic Al's oil that had equilibrated in the anaerobic chamber 72+ hrs was then carefully layered on top of each deoxyHb sample up to the brim of the sample cup. Each Reacti-Vial with sample was then sealed with a septum for transport to the chameleon for cryoEM grid preparation.

MoFeP Samples:

MoFeP that had been flash frozen in liquid nitrogen was transferred into a Coy Laboratories anaerobic chamber and exchanged into reaction buffer (20 mM Tris, pH 8.0, 25 mM NaCl, anaerobic). MoFeP was concentrated with a 100 kDa Microcon centrifugal filter (Millipore) to ∼3 mg/mL and syringed-filtered (0.2 μM filter). Protein concentration was verified using an iron chelation assay and diluted to 30 μM.

Stock detergent solutions of CHAPSO, fluorinated octylmaltoside (FOM), amphipol A8-35, and Brij-35 were prepared in separate vials and degassed in an anaerobic chamber. A detergent cocktail solution comprising 0.110% (w/v) CHAPSO, 0.00964% (w/v) FOM, 0.12% (w/v) A8-35, 0.006%

(v/v) Brij-35, and either 0 or 40 mM NaDT was prepared. 10 μL of the detergent cocktail mix was then carefully mixed with 10 μL of 30 μM MoFeP (1:1 final ratio) and 15 μL of the mixture was located into a chameleon sample cup within a 3 mL glass Reacti-Vial. The MoFeP sample without dithionite was then sealed within the Reacti-Vial using a septum for transport to the chameleon for cryoEM grid preparation. ~70 μL of anaerobic Al's oil was then carefully layered above the MoFeP sample containing 20 mM NaDT up to the brim of the sample cup and the Reacti-Vial was sealed for transport to the chameleon for cryoEM grid preparation.

Chameleon Preparation:

All samples were prepared and immediately taken to the chameleon for grid preparation. All steps were performed using a SPT Labtech chameleon. The chameleon was prepared according to established protocols. Liquid ethane was maintained within a temperature range of -173 to -175 °C and the humidity shroud was maintained at >75% relative humidity (RH) during grid vitrification. For each sample, 2-4 chameleon self-wicking grids (Quantifoil Active 300 mesh; Quantifoil) were loaded into the instrument and glow discharged for 40-45 seconds at 12 mA. Once the instrument glow discharged the grids, the Reacti-Vial was unsealed, and the chameleon sample cup was immediately and carefully loaded into the instrument. 7 μL of sample was immediately aspirated into the dispenser and subsequently tested for proper dispensing within the chameleon software before sample deposition on to the grid. At this stage, some Al's oil may remain on the dispenser tip blocking sample spray/deposition. Obvious signs of oil included oil-like features when "inspect dispenser" was selected as well as lack of sample droplets when reviewing dispenser testing in the software **(Fig. S1)**. If that was the case, then initially the dispense amplitude (under Advanced Troubleshooting) was increased 2-fold (~800) to attempt to remove the oil from the dispenser tip. The amplitude was consistently increased by 100 until sample droplets appear, or an amplitude of 1200 was reached. If droplets were observed, the amplitude can be decreased back down to proper working conditions (~400) to obtain the recommended 5 droplets. If, however, the oil persisted even with increase in sample dispense amplitude to 1200, then the "Mini Prime" option was selected followed by "Wipe Dispenser." At this point, the line should have been fully purged and relieved of oil. The amplitude of the dispenser was then adjusted until the recommended 5 droplets were obtained. Once ideal sample dispensing conditions were obtained, grids were frozen with 300-900 ms plunge time using 40-150 s glow discharge times. Of note, shorter wicking times required longer glow discharge times for proper ice thinning. The time from sample loading to vitrification of the first grid was 90-120 s. Each subsequent grid was frozen within 60-120 s of the first. We prioritized the first grid during screening and collection.

Hb oxygen diffusion assay

For assessing oxygen diffusion into our samples, deoxyHb was prepared as described above and diluted with anaerobic PBS and NaDT to generate 1 mL each of the following samples: 1.5 μM deoxyHb with 25 μM NaDT, 1.5 μM deoxyHb with 20mM NaDT; and 1.5 μM deoxyHb with 60mM NaDT. The mixed samples were then transferred to a degassed plastic spectrophotometry cuvette and either measured as is or layered with anaerobic Al's oil that approximates the height of the oil layer added to the sample cup, approximately 500 μL. These samples were sealed and then transported out of the anaerobic environment and immediately placed into an Agilent 8453 UV-Vis spectrometer blanked with 1x PBS. For each sample, the cuvette was unsealed absorbance from 350 nm to 700 nm was measured with a time scan rate of 12000 nm/min at a wavelength interval of 2.5 nm for 20 minutes. The change in the absorbance of the Soret peak maximum at 415 nm was plotted vs time.

CryoEM data collection

All data was acquired at UCSD's CryoEM Facility using a Titan Krios G4 (ThermoFisher Scientific) operating at 300 kV equipped with a Selectris-X energy filter (ThermoFisher Scientific). All images were collected at a nominal magnification of 165,000x in EF-TEM mode (with a calibrated pixel size of 0.735Å) on a Falcon4 direct electron detector (ThermoFisher Scientific) using a 10 eV slit width. Micrographs were acquired in EER format with a cumulative electron exposure of 60 electrons/Å^2 with a defocus range of -1 to -2.0 μm. Data was collected automatically using EPU2 (ThermoFisher Scientific) with aberration free image shift. Data was monitored live using cryoSPARC Live (Structura Bio) where movies were patch motion corrected and patch CTF estimated on the fly. Micrographs with a CTF estimation worse than 7 Å and/or a cumulative motion of more than 150 pixels were discarded. Hb datasets: the oiled met Hb dataset contained 2,384 micrographs, while the non-oiled contained 2,847 micrographs. The "no" NaDT and low NaDT oxy Hb datasets contained 2,475 and 1,538 micrographs, respectively, the partial oxy Hb dataset contained 3,925 micrographs, and the deoxyHb dataset contained 2,220 micrographs. MoFeP datasets: the oxidized MoFeP dataset was two imaging session where dataset 1 contained 1067 micrographs and dataset 2 contained 1975 micrographs, while the reduced MoFeP dataset contained 2,000 micrographs.

CryoEM data processing

For all data sets (Hb and MoFeP), initial particle picking was performed within cryoSPARC Live using templates. These picks were then exported to cryoSPARC and downstream processing for both Hb and MofeP proceeded as described below.[54]

Hb data processing:

For all Hb data sets (Oiled, Non-Oiled, 25μM NaDT, 5 mM NaDT, 20mM NaDT, 60mM NaDT), particles were extracted at a box size of 256 pixels and Fourier cropped to 64 pixels at 2.94 Å/pixel. These particles were then subjected to one round of two-dimensional (2-D) classification, where

obvious Hb tetramer classes were chosen to move forward. The selected particles we re-extracted and recentered using the same box and Fourier cropping and subjected to a second round of 2-D classification. The final set of selected particles from the 2-D classifications were then subjected to a non-uniform (NU) refinement using C2 symmetry and a starting model from EMD-0407 (metHb) lowpass filtered to 15 Å and clipped to the same box size.[39] The particle stack was then subjected to heterogeneous refinement with one volume being the volume from the previous NU refinement, the EMD-0407 volume, and the volume from EMD-4877 (20S proteasome).[39,55] The particles that contributed to the best volume that resembled Hb tetramer were selected and extracted at a box size of 256 pixels with a Fourier crop to 128 pixels at 1.47 Å/pixel. These re-extracted particles were subjected to a NU-refinement (C2 symmetry) using the selected volume from the heterogeneous refinement low-pass filtered to 10 Å as an initial model to assess overall particle quality before fully unbinning the particles. Following this refinement, the particles were re-extracted with a box size of 256 pixels at 0.735 Å/pixel. These particles were then used for an *ab initio* model generation (2-classes) with a max resolution of 4 Å. The class with the best continuous density and completeness was chosen for a subsequent NU-refinement (C2 symmetry) using the best *ab initio* volume low-pass filtered to 10 Å as an initial model. Additionally, this refinement optimized per particle defocus and aberrations. Finally, due to signal delocalization in real space that leads loss of signal in real space as well as CTF aliasing in reciprocal space, we performed a final extraction at a box size of 352 pixels at 0.735 Å/pixel. We then performed a NU-refinement with C2 symmetry and without (real space windowing off) with per particle defocus and aberration refinement turned on. These last two refinements lead to the final densities that were used for analysis and phenix.resolve_cryo_em.[47]

MoFeP data processing:

For the oxidized MoFeP datasets, each micrograph set was template picked using templates generated from a previously published MoFeP volume[15] and extracted with a box size of 384 pixels Fourier cropped to 64 pixels at 4.41 Å/pixel. Dataset 1 particles were subjected to a 2-D classification. Particles in the best MoFeP classes were selected used for ab initio (2 classes) model generation. The *ab initio* class that provided the most complete MoFeP density was chosen, and the particles associated with this class were carried forward to a NU-refinement. We noticed that this resulting density had some streaking indicating the presence of destructive particles, hence we ran a second 2-D classification. We then performed another 2-class *ab initio* model generation where particles in the best class was used for a NU-refinement. The particles were re-centered and re-extracted with a box size of 384 pixels without any Fourier cropping resulting in a pixel size of 0.735 Å/pixel. These unbinned particles were subjected to a NU-refinement using the previous *ab initio* volume was as an initial model with per particle defocus and aberration refinement turned on (real space windowing off). The particles were then subjected to Reference-Based Motion Correction (RBMC) and a final NU-refinement was performed using the same parameters as the previous NU-refinement before combining particles. For Dataset 2, we used a more simplified workflow that utilized a single round of 2-D classification followed by a 2-class *ab initio* model generation. Particles in the best class were then used for NU-refinement. Particles from Dataset 1 and Dataset 2 were then combined and re-extracted at a box size of 384 pixels at 0.735 Å/pixel. We then performed a NU-refinement on these combined particles, using the volume from the last NU-refinement of Dataset 1, with per particle defocus and aberration refinement turned on (real space windowing off). The combined particles were subjected to RBMC followed by a NU-refinement using the same parameters as the previous NU-refinement with C2 symmetry and without. The densities from these NU-refinements were then used for analysis and phenix.resolve_cryo_em.

Processing of the reduced MoFeP dataset was performed similarly as described for Dataset 2 of the oxidized MoFeP structure with the following exception: the "Import Beam Shift" tool was used to separate the particles into their different aberration free image shift groups (80 in total) for use during aberration refinement during NU-refinement.

Refinement

All models presented in this work were generated using a similar workflow. All final volumes were subjected to the phenix.resolve_cryo_em density modification tool, where only half maps and sequence file was supplied. For our metHb, oxyHb, mixed Hb, and deoxyHb maps, PDB: 6NBC was fit into the resulting RESOLVE density and manually adjusted in COOT. For the oxidized and reduced MoFeP structures, PDB: 7UT7 was fit into the resulting RESOLVE density and manually adjusted in COOT Oxygens were manually placed in the OxyHb and mixed Hb structures. Real space refinement was performed using Phenix.[56] Parameter files for the heme-oxygen, P-cluster (P^N or P^2+), and homocitrate-FeMoco ligands were used during refinement. Phenix douse was then used on the resulting model to identify and add waters. The model was then checked for accuracy in COOT and a final real space refinement was performed against the sharpened map from cryoSPARC **(Table 1)**.

Data Availability

Structural models have been deposited in the Protein Data Bank with accession codes 9CQO/9CQP (non-oiled metHb, C1/C2), 9CQQ/9CQR (oiled metHb, C1/C2), 9CQM/9CQN (very low NaDT OxyHb, C1/C2), 9CQS/9CQT (low NaDT oxyHb, C1/C2), 9CQU (partially oxygenated Hb, C1), 9CQV/9CQW (deoxyHb, C1/C2), 9CQX/9CQY (oxidized MoFeP, C1/C2), and 9CQZ/9CR0 (reduced MoFeP). The corresponding cryo-EM maps are available at the Electron Microscopy Data Bank (www.ebi.ac.uk/emdb/) with accession codes

EMD-45817/EMD-45818 (non-oiled metHb, C1/C2), EMD-45819/EMD-45820 (oiled metHb, C1/C2), EMD-45815/EMD-45816 (very low NaDT oxyHb, C1/C2), EMD-45821/EMD-45822 (low NaDT oxyHb, C1/C2), EMD-45823 (partially oxygenated Hb, C1), EMD-45824/ EMD-45825 (deoxyHb, C1/C2), EMD-45826/ EMD-45827 (oxidized MoFeP, C1/C2), EMD-45828/ EMD-45829 (reduced MoFeP, C1/C2). All other data are available in the main text or the supplementary materials.

Ethics Declaration

The authors declare no competing interests.

Acknowledgements

We are grateful to Prof. Kevin Corbett for providing valuable feedback on this manuscript, and the entirety of the Herzik lab for facilitating insightful discussions. The authors acknowledge the facilities, along with the scientific and technical assistance of the staff of the cryo-EM facility at UC San Diego, Dr. Mariusz Matyszewski and Dr. Inga Kuschnerus. We also thank Brendan Dennis, Kevin Smith, and the UCSD Physics Computing Facility for their insights and support. Molecular graphics and analyses were performed with UCSF ChimeraX, developed by the Resource for Biocomputing, Visualization, and Informatics at the University of California, San Francisco (UCSF), with support from National Institutes of Health (NIH) grant R01-GM129325 and the Office of Cyber Infrastructure and Computational Biology, National Institute of Allergy and Infectious Diseases. This work was supported from the NIH grant 5R35GM138206-05. SMN is supported by the Interfaces Graduate Training Program at UCSD. BC is supported by Goeddel Family Technology Sandbox Fellowship.

References

(1) Rutledge, H. L.; Tezcan, F. A. *Chemical Reviews* **2020**, *120*, 5158–5193.

(2) Klusch, N.; Dreimann, M.; Senkler, J.; Rugen, N.; Kühlbrandt, W.; Braun, H.-P. *Nature Plants* **2022**, *9*, 142–156.

(3) Cammack, R.; Rao, K.; Hall, D. *Biosystems* **1981**, *14*, 57–80.

(4) Imlay, J. A. *Molecular Microbiology* **2006**, *59*, 1073–1082.

(5) Nicolet, Y.; Fontecilla-Camps, J. C. *Iron-Sulfur Clusters in Chemistry and Biology* **2014**, Publisher: Walter de Gruyter GmbH & Co KG.

(6) Cherrier, M. V.; Vernède, X.; Fenel, D.; Martin, L.; Arragain, B.; Neumann, E.; Fontecilla-Camps, J. C.; Schoehn, G.; Nicolet, Y. *Biomolecules* **2022**, *12*, 441.

(7) Warmack, R. A.; Wenke, B. B.; Spatzal, T.; Rees, D. C. *Nature Protocols* **2024**, DOI: 10.1038/s41596-024-00973-5.

(8) Senda, M.; Senda, T. *Biophysical Reviews* **2018**, *10*, 183–189.

(9) Winter, M. B.; Herzik, M. A.; Kuriyan, J.; Marletta, M. A. *Proceedings of the National Academy of Sciences* **2011**, *108*, DOI: 10.1073/pnas.1114038108.

(10) Tezcan, F. A.; Kaiser, J. T.; Howard, J. B.; Rees, D. C. *Journal of the American Chemical Society* **2015**, *137*, 146–149.

(11) Kovaleva, E. G.; Lipscomb, J. D. *Science* **2007**, *316*, 453–457.

(12) Sato, N.; Uragami, Y.; Nishizaki, T.; Takahashi, Y.; Sazaki, G.; Sugimoto, K.; Nonaka, T.; Masai, E.; Fukuda, M.; Senda, T. *Journal of Molecular Biology* **2002**, *321*, 621–636.

(13) Hsieh, Y.-C.; Liu, M.-Y.; Le Gall, J.; Chen, C.-J. *Acta Crystallographica Section D Biological Crystallography* **2005**, *61*, 780–783.

(14) Senda, M.; Kishigami, S.; Kimura, S.; Fukuda, M.; Ishida, T.; Senda, T. *Journal of Molecular Biology* **2007**, *373*, 382–400.

(15) Rutledge, H. L.; Cook, B. D.; Nguyen, H. P. M.; Herzik, M. A.; Tezcan, F. A. *Science* **2022**, *377*, 865–869.

(16) Warmack, R. A.; Maggiolo, A. O.; Orta, A.; Wenke, B. B.; Howard, J. B.; Rees, D. C. *Nature Communications* **2023**, *14*, 1091.

(17) Xu, D.; Thomas, W. C.; Burnim, A. A.; Ando, N. Conformational Landscapes of a Class I Ribonucleotide Reductase Complex during Turnover Reveal Intrinsic Dynamics and Asymmetry, en, 2024.

(18) Nakanishi, A.; Kishikawa, J.-i.; Mitsuoka, K.; Yokoyama, K. *Journal of Biological Chemistry* **2023**, *299*, 102884.

(19) Chua, E. Y.; Mendez, J. H.; Rapp, M.; Ilca, S. L.; Tan, Y. Z.; Maruthi, K.; Kuang, H.; Zimanyi, C. M.; Cheng, A.; Eng, E. T.; Noble, A. J.; Potter, C. S.; Carragher, B. *Annual Review of Biochemistry* **2022**, *91*, 1–32.

(20) Han, B.-G.; Avila-Sakar, A.; Remis, J.; Glaeser, R. M. *Current Opinion in Structural Biology* **2023**, *81*, 102646.

(21) Chiu, W.; Schmid, M. F.; Pintilie, G. D.; Lawson, C. L. *Journal of Biological Chemistry* **2021**, *296*, 100560.

(22) Glaeser, R. M.; Han, B.-G. *Biophysics Reports* **2017**, *3*, 1–7.

(23) D'Imprima, E.; Floris, D.; Joppe, M.; Sánchez, R.; Grininger, M.; Kühlbrandt, W. *eLife* **2019**, *8*, e42747.

(24) Tan, Y. Z.; Baldwin, P. R.; Davis, J. H.; Williamson, J. R.; Potter, C. S.; Carragher, B.; Lyumkis, D. *Nature Methods* **2017**, *14*, 793–796.

(25) Khoroshilova, N.; Popescu, C.; Münck, E.; Beinert, H.; Kiley, P. J. *Proceedings of the National Academy of Sciences* **1997**, *94*, 6087–6092.

(26) Boehme, D. E.; Vincent, K.; Brown, O. R. *Nature* **1976**, *262*, 418–420.

(27) Dandey, V. P. et al. *Nature Methods* **2020**, *17*, 897–900.

(28) Jain, T.; Sheehan, P.; Crum, J.; Carragher, B.; Potter, C. S. *Journal of Structural Biology* **2012**, *179*, 68–75.

(29) Razinkov, I.; Dandey, V. P.; Wei, H.; Zhang, Z.; Melnekoff, D.; Rice, W. J.; Wigge, C.; Potter, C. S.; Carragher, B. *Journal of Structural Biology* **2016**, *195*, 190–198.

(30) Dandey, V. P.; Wei, H.; Zhang, Z.; Tan, Y. Z.; Acharya, P.; Eng, E. T.; Rice, W. J.; Kahn, P. A.; Potter, C. S.; Carragher, B. *Journal of Structural Biology* **2018**, *202*, 161–169.

(31) Feng, X.; Fu, Z.; Kaledhonkar, S.; Jia, Y.; Shah, B.; Jin, A.; Liu, Z.; Sun, M.; Chen, B.; Grassucci, R. A.; Ren, Y.; Jiang, H.; Frank, J.; Lin, Q. *Structure* **2017**, *25*, 663–670.e3.

(32) Levitz, T. S.; Weckener, M.; Fong, I.; Naismith, J. H.; Drennan, C. L.; Brignole, E. J.; Clare, D. K.; Darrow, M. C. *Frontiers in Molecular Biosciences* **2022**, *9*, 903148.

(33) McGuire, K. L.; Cook, B. D.; Narehood, S. M.; Herzik, M. A. Tuning ice thickness using the chameleon for high-quality cryoEM data collection, en, 2024.

(34) Levitz, T. S.; Brignole, E. J.; Fong, I.; Darrow, M. C.; Drennan, C. L. *Journal of Structural Biology* **2022**, *214*, 107825.

(35) Eaton, W. A.; Henry, E. R.; Hofrichter, J.; Bettati, S.; Viappiani, C.; Mozzarelli, A. *IUBMB Life* **2007**, *59*, 586–599.

(36) Alayash, A. I. *Frontiers in Medical Technology* **2022**, *4*, 1068972.

(37) Weigand, M. R. H.; Gómez-Pastora, J.; Kim, J.; Kurek, M. T.; Hickey, R. J.; Irwin, D. C.; Buehler, P. W.; Zborowski, M.; Palmer, A. F.; Chalmers, J. J. *PLOS ONE* **2021**, *16*, ed. by Reid, C. W., e0257061.

(38) Berkeley, R. F.; Cook, B. D.; Herzik, M. A. *Frontiers in Molecular Biosciences* **2024**, *11*, 1404885.

(39) Herzik, M. A.; Wu, M.; Lander, G. C. *Nature Communications* **2019**, *10*, 1032.

(40) D'Arcy, A.; Mac Sweeney, A.; Stihle, M.; Haber, A. *Acta Crystallographica Section D Biological Crystallography* **2003**, *59*, 396–399.

(41) Chayen, N. E. In *Macromolecular Crystallography Protocols*, Walker, J. M., Doublié, S., Eds., Series Title: Methods in Molecular Biology; Humana Press: Totowa, NJ, 2007; Vol. 363, pp 175–190.

(42) Als Oil (50:50 Paraffin:Silicon).

(43) Stokes, T. M. *Molecular Reproduction and Development* **2009**, *76*, 1178–1187.

(44) Meng, F.; Alayash, A. I. *Analytical Biochemistry* **2017**, *521*, 11–19.

(45) Lambeth, D. O.; Palmer, G. *Journal of Biological Chemistry* **1973**, *248*, 6095–6103.

(46) Park, S.-Y.; Yokoyama, T.; Shibayama, N.; Shiro, Y.; Tame, J. R. *Journal of Molecular Biology* **2006**, *360*, 690–701.

(47) Terwilliger, T. C.; Ludtke, S. J.; Read, R. J.; Adams, P. D.; Afonine, P. V. *Nature Methods* **2020**, *17*, 923–927.

(48) Warmack, R. A.; Rees, D. C. *Molecules* **2023**, *28*, 7952.

(49) Tezcan, F. A.; Kaiser, J. T.; Mustafi, D.; Walton, M. Y.; Howard, J. B.; Rees, D. C. *Science* **2005**, *309*, 1377–1380.

(50) Owens, C. P.; Katz, F. E. H.; Carter, C. H.; Luca, M. A.; Tezcan, F. A. *Journal of the American Chemical Society* **2015**, *137*, 12704–12712.

(51) Einsle, O.; Tezcan, F. A.; Andrade, S. L. A.; Schmid, B.; Yoshida, M.; Howard, J. B.; Rees, D. C. *Science* **2002**, *297*, 1696–1700.

(52) Kim, J.; Woo, D.; Rees, D. C. *Biochemistry* **1993**, *32*, 7104–7115.

(53) Rutledge, H. L.; Rittle, J.; Williamson, L. M.; Xu, W. A.; Gagnon, D. M.; Tezcan, F. A. *Journal of the American Chemical Society* **2019**, *141*, 10091–10098.

(54) Punjani, A.; Rubinstein, J. L.; Fleet, D. J.; Brubaker, M. A. *Nature Methods* **2017**, *14*, 290–296.

(55) Toste Rêgo, A.; Da Fonseca, P. C. *Molecular Cell* **2019**, *76*, 138–147.e5.

(56) Liebschner, D. et al. *Acta Crystallographica Section D Structural Biology* **2019**, *75*, 861–877.